C: Energy Conversion and Storage; Energy and Charge Transport

Band Edge Tailoring in Few-layer Two-dimensional Molybdenum Sulfides/Selenides Alloys

Yi-Rung Lin, Wen-Hui Cheng, Matthias H. Richter, Joseph S DuChene, Elizabeth A. Peterson, Cora M. Went, Zakaria Y. Al Balushi, Deep Jariwala, Jeffrey B. Neaton, Li-Chyong Chen, and Harry A Atwater

J. Phys. Chem. C, **Just Accepted Manuscript** • DOI: 10.1021/acs.jpcc.0c04719 • Publication Date (Web): 14 Sep 2020

Band Edge Tailoring in Few-layer Two-dimensional Molybdenum Sulfides/Selenides Alloys

Yi-Rung Lin[1,2,3,4], Wen-Hui Cheng[1,2], Matthias H. Richter[2,5], Joseph S. DuChene[1,2], Elizabeth A. Peterson[6,7], Cora M. Went[8], Zakaria Y. Al Balushi[1,9], Deep Jariwala[1,#] Jeffrey B. Neaton[6,10,11], Li-Chyong Chen[3,4] and Harry A. Atwater*[1,2]

[1]Thomas J. Watson Laboratory of Applied Physics, California Institute of Technology, Pasadena, California 91125 United States

[2]Joint Center for Artificial Photosynthesis, California Institute of Technology, Pasadena, California 91125 United States

[3]Center for Condensed Matter Sciences, National Taiwan University, No. 1, Sec. 4, Roosevelt Road, Taipei, 10617, Taiwan

[4]Center of Atomic Initiative for New Materials, National Taiwan University, No. 1, Sec. 4, Roosevelt Road, Taipei, 10617, Taiwan

[5]Division of Chemistry and Chemical Engineering, California Institute of Technology, Pasadena, CA 91125, USA

[6]Department of Physics, University of California, Berkeley, California, 94720, USA

[7]Joint Center for Artificial Photosynthesis, Lawrence Berkeley National Laboratory, Berkeley, California 94720, USA

[8]Department of Physics, California Institute of Technology, Pasadena, CA 91125, USA

[9]The Resnick Sustainability Institute, California Institute of Technology, Pasadena, California 91125 United States

[10]Molecular Foundry, Lawrence Berkeley National Laboratory, Berkeley, California 94720, USA

[11]Kavli Energy NanoSciences Institute at Berkeley, Berkeley, California 94720, USA

Current address: Electrical and Systems Engineering, University of Pennsylvania, Philadelphia, PA, 19104, USA

ABSTRACT

Chemical alloying is a powerful approach to tune the electronic structure of semiconductors, and has led to the synthesis of ternary and quaternary two-dimensional (2D) dichalcogenide semiconductor alloys (*e.g*. $MoSSe_2$, $WSSe_2$ etc.). To date, most studies have been focused on determining the chemical composition by evaluating the optical properties, primarily via photoluminescence and reflection spectroscopy of these materials in the 2D monolayer limit. However, a comprehensive study of alloying in multilayer films with direct measurement of electronic structure, combined with first principles theory, is required for a complete understanding of this promising class of semiconductors. We have combined first-principles density functional theory calculations with experimental characterization of $MoS_{2(1-x)}Se_{2x}$ (where x ranges from 0 to 1) alloys using X-ray photoelectron spectroscopy to evaluate the valence and conduction band edge positions in each alloy. Moreover, our observations reveal that the valence band edge energies for molybdenum sulfide/selenide alloys increase as a function of increasing selenium concentration. These experimental results agree well with the results of density functional theory calculations showing a similar trend in calculated valence band edges. Our studies suggest that alloying is an effective technique for tuning the band edges of transition-metal dichalcogenides, with implications for applications such as solar cells and photoelectrochemical devices.

▪ INTRODUCTION

Two-dimensional (2D) transition-metal dichalcogenides (TMDCs) with the general formula MX_2 (M = Mo, W; X = S, Se, Te) have been widely explored as a material system for nanoelectronics, optoelectronics, and catalysis. Their layered structure and van der Waals bonding determine their electron transport properties and gives rise to strong exciton confinement.[1–4] In particular, TMDCs exhibit layer-dependent optoelectronic properties from a direct energy gap (monolayer) to an indirect energy gap (multilayer and bulk), which makes this class of semiconductors versatile for optoelectronic devices. TMDCs are also catalytically active for the hydrogen evolution reaction (HER), due to the presence of chalcogen vacancies and active edge sites, as well as suitable band edge positions relative to the reduction potential for the HER.[5–12] For instance, MoS_2 is well-known for its superior HER performance in activity and stability, and after selenium incorporation, $MoS_{2(1-x)}Se_{2x}$ exhibits further enhanced catalytic HER performance.[13,14] To date many studies have focused on the optoelectronic properties of monolayer TMDCs, while a comprehensive study of the ground state electronic structure of few-layer TMDC alloys remains lacking. Earlier theoretical studies reveal that the conduction band edge of monolayer MoS_2 is well aligned to the energy level for CO_2 reduction (CO_2R) to methane, while the valence band edge of $MoSe_2$ is well-aligned for water oxidation.[15–19] Thus, the band edge position of MoS_2 is used as an indicator to predicting its catalytic activity in (photo)electrochemical CO_2R. Synthesis of TMDC substitutional alloys containing Mo, W, S, and Se has been achieved via chemical vapor deposition (CVD) or chemical vapor transport (CVT).[20-31] Several studies have focused on the synthesis, electronic structure, and optical properties of monolayer 2D MoS_2, $MoSe_2$, and MoSSe.[32–35] Despite much progress, studies of the influence of TMDC alloy composition on electronic properties are very limited. Although several studies have used first-principles calculations to understand the electronic structure and optical properties of a variety of 2D van der Waals (vdW) heterostructures,[20,36–41] they have focused on the electronic band structure of monolayer TMDCs. Few-layer TMDCs and their alloys have rarely been examined. Furthermore, most of these prior theoretical studies are independent and have failed to link electronic structure calculations with a direct experimental measurement of the band positions of TMDC alloys. Therefore, a combined experimental and theoretical investigation of the effect of elemental composition on electronic band structure is needed to expand our knowledge of few-layer TMDC materials and enable future optoelectronic and photoelectrochemical applications.

We employ a combined experimental and theoretical approach to the synthesis and characterization of 4-layer (4L) $MoS_{2(1-x)}Se_{2x}$ ($0 < x < 1$) alloys and relate chemical composition to the ground state electronic structure of the alloy. Our study provides direct experimental measurements of the valence band (VB) and conduction band (CB) positions of few-layer MoSSe alloys in the multilayer thickness regime supported by first-principles calculations. Significantly, our theoretical calculations consider three distinct atomic configurations of the synthesized MoSSe heterostructures that have not been considered previously. Our correlated experimental and theoretical results demonstrate that all three configurations exhibit an overall upward trend in VB and CB position as the Se fraction increases in the alloys. Overall, our results suggest that chemical alloying enables the systematic tuning of the band edges of molybdenum sulfide/selenide alloys, with implications for a variety of catalytic applications.[32,42–47]

▪ METHODS

2.1 Synthesis of MOCVD-grown MoS_2. The synthesis of monolayer to few-layer MoS_2 was carried out in a 5 inch (outer diameter) hot-wall quartz tube furnace. We synthesized monolayer MoS_2 on a 4-inch Si wafer with 298 nm thick thermal SiO_2 using metal-organic chemical vapor deposition (MOCVD). Molybdenum hexacarbonyl (MHC) and diethyl sulfide (DES) were selected as chemical precursors for Mo and S, respectively, and then introduced to the furnace by flowing an Ar carrier gas through the bubblers. H_2 and Ar background gases were introduced into the chamber as the carrier gases using separate lines. In the growth process, a 4-inch Si/SiO_2 wafer was placed on the quartz substrate holder at the center zone of the furnace. We controlled the chamber pressure at 5 torr, growth temperature of 600 °C and growth time of 3 hrs. The flow rates of precursors were 10 sccm for the Ar flowing through the MHC bubbler and 30 sccm for the Ar flowing through the DES bubbler, 85 sccm for H_2, and 500 sccm for Ar, which were regulated by individual mass flow controllers (MFCs). The bubbler pressures for the precursors were 250 Torr for MHC and 200 Torr for DES. In the 3hr growth time, we were able to achieve the continuous multilayer MoS_2 growth. MHC: STREM 42-1350, DES: Sigma Aldrich 107247.

2.2. Thermal Selenization of As-grown MoS_2 to Form $MoS_{2(1-x)}Se_{2x}$. The selenization process was performed under a three-zone quartz tube furnace with 4.5-inch diameter. Selenium powder (Sigma-Aldrich, -100 mesh, 99.99% trace metal basis) was used as the precursor for CVD reaction. In each selenization experiment, the selenium powders with the fixed amount (1.18 g) were placed

in a quartz boat at the upstream side of the furnace and then heated up to 300 °C with flowing a H_2/N_2 (1:9) has mixture at the pressure of 400 torr. The selenium powders were volatile under 300°C and became selenium vapors, which were carried with N_2/H_2 mixture gases to the downstream. Each as-grown quadrilayer MoS_2 on SiO_2/Si sample was cut into 1 x 1 cm^2, and placed on the quartz substrate holder at the center of a hot wall furnace for selenization at 600 to 800 °C for 15~60 minutes. When temperature > 600°C, the selenium vapors reacted with H_2 to form H_2Se(g), which further reacted with MoS_2 samples and form $MoS_{2(1-x)}Se_{2x}$. The control of selenium concentration in $MoS_{2(1-x)}Se_{2x}$ (x = 0.12, 0.18, 0.23, 0.26, and 1) depended on various selenization temperature and time, which were 600°C, 650°C, 700°C, 750°C for 15 minutes and 800°C for 60 minutes, respectively. After synthesis, the furnace was naturally cooled down to room temperature.

2.3 X-ray Photoelectron Spectroscopy Analysis. XPS measurements were performed using a Kratos Axis Ultra (and Surface Science M Probe) system with a base pressure of < $1x10^{-9}$ mtorr. A monochromatic Al K_α ($\hbar\omega$ = 1486.69 eV) source with a power of 150 W was used for all measurements.

2.3.1. Chemical Compositions of $MoS_{2(1-x)}Se_{2x}$. We performed the X-ray photoelectron spectroscopy (XPS) to characterize the chemical compositions and valence-band positions of $MoS_{2(1-x)}Se_{2x}$. The information we acquired here are macroscopic, which averaged the local information since the spot size was about several hundred microns. Core levels where calibrated to Au 4f (84 eV) which was deposited on the SiO_2 substrate and the corresponding binding energy of the Si^{4+} 2p core level (102.7 eV) was used as a reference for all subsequent measurements. Overview scans were collected with a pass energy of 160eV whereas detailed scans were performed with a pass energy of 20 eV. CasaXPS was used for background removal (Shirley type) and peak fitting. For the calculation of atomic ratios and the peak intensities, both obtained from peak fitting, were corrected by the analyzer transmission function (TF) and the respective atomic sensitivity factors (ASF) of the core levels.

2.3.2 Valence Band Maximum (VBM) Measurement. The valence band edge is the region close to zero binding energy (maximum kinetic energy). The valence band maximum position (VBM) was determined by fitting a fermi distribution to the edge. The function of the Fermi-Dirac distribution is described as follows:

$$f(E) = \frac{A}{1 + e^{\frac{E - VBM}{k_B T \cdot B}}}$$

where k_B is Boltzmann's constant, T is the absolute temperature, A as a step height parameter, B as peak broadening, and VBM as the valence band maximum.[48]

2.3.3 Work Function Measurement The work function of the sample was determined by measuring the secondary electron cutoff of the sample while biasing the sample with a stabilized voltage source (+9V) to overcome the work function of the analyzer. The spectra were then corrected by the applied bias, and the position of the secondary electron cutoff edge was determined by the interception of a linear fit to the background and a linear fit to the edge. In an intensity vs. kinetic energy plot, this value at the intersection will directly yield the value of work function; for binding energy scale, the value has to be converted by the photon energy.

2.4. Optical Band Gap Measurement. In order to reduce possible damage during the film transfer process and obtain the information directly from the sample, we perform ellipsometry (J.A. Woollam Co. model VASE) measurements with thin film on glassy carbon support or SiO_2/Si substrate. The angle of incident was chosen to be 65°, 70°, and 75°. We then extract the optical constant n (refractive index) and k (extinction coefficient) of the synthesized $MoS_{2(1-x)}Se_{2x}$ samples. The optical band gaps are defined at the rise of the extinction coefficient.

2.5. Materials and Morphological Characterizations. Raman and room temperature photoluminescence (PL) measurements in ambient condition using Renishaw M1000 Micro Raman Spectrometer System with 514 nm laser excitation with 100X objective and 1% power density (spot size is about 1μm). For wavelength calibration, we measured the Si peak at 520.7 cm^{-1} on an undoped silicon wafer as the reference. The emitted Stokes Raman signal was collected by a 0.85 N.A. of 100x objective from Leica in 2400 lines/mm grating for Raman measurement and 1800 lines/mm grating for PL measurement. Scanning electronic microscopy **(**SEM) images were obtained with a FEI Nova NanoSEM 450 microscope.

2.6 DFT Calculations. First-principles ionic and electronic structure calculations were performed using density functional theory (DFT) with a plane-wave basis and projector augmented wave (PAW) potentials[49] as implemented by the Vienna *ab-initio* simulation package (VASP).[50,51] All calculations are performed in the generalized gradient approximation as implemented by Perdew, Burke and Ernzerhof (PBE),[52] with additional van der Waals corrections using rev-vdW-

DF2 to incorporate dispersion forces.[53] For homogeneous alloys and vertical heterostructures a plane-wave energy cut-off of 750 eV was used with a 10x10x1 Gamma-centered k-point mesh for structural relaxations, band structures and slab calculations. The most stable homogeneous alloys were determined by considering all symmetrically distinct arrangements of S and Se in a 2x2x1 bulk supercell. A quadrilayer slab with 20 Å of vacuum was used for structural relaxation of the vertical heterostructures. All forces were converged to < 0.001 eV/Å. Calculations of the electrostatic potential along the c-axis of quadrilayer slabs with 20 Å of vacuum for each system were performed to determine absolute band edges. The absolute position of the Fermi energy relative to the electrostatic energy of the vacuum region was taken as the valence band maximum (VBM). The conduction band minimum (CBM) was determined by adding the bulk band structure to the slab VBM. For small lateral domain calculations bulk structural relaxations were performed with a plane-wave energy cut-off of 750 eV used with a 2x2x1 Gamma-centered k-point mesh on a 10x10x1 supercell of MoS_2 with regions of $MoSe_2$ of varying size. All forces were converged to < 0.01 eV/Å. A quadrilayer slab calculation with 15 Å of vacuum was performed using a 600 eV energy cut-off and a 2x2x1 k-point mesh to determine the absolute positions of the VBM and CBM. An empirical correction scheme was further applied to the calculated band edges. The differences between the experimental band edges and DFT band edges for pristine MoS_2 and $MoSe_2$ were calculated, then linearly interpolated across the alloys as a function of Se content x in order to generate empirical corrections for the DFT band edges.

▪ RESULTS AND DISCUSSION

The synthesis of two-dimensional molybdenum disulfide (MoS_2) thin-films was performed via metal-organic chemical vapor deposition (MOCVD) on four-inch silicon (Si) wafers with 298-nm-thick thermal oxide (SiO_2) (Figure 1a). The MoS_2 film thickness varied as a function of distance across the wafer substrate from multilayered films (> 5 layers) to sub-monolayer flakes. The microstructure of as-grown MoS_2 films was examined under scanning electron microscopy (SEM). SEM images from different portions of the substrate are shown in Figure 1b and Figure 1c, where sub-monolayer MoS_2 islands can be observed with lateral sizes of approximately 20 nm. Previously, many studies have reported the optical properties, such as band gap of monolayer

MoS_2 is about 1.8 eV and few-layer samples range from 1.2-1.6 eV. We further characterized the MoS_2 film thickness and its crystallinity using Raman spectroscopy and photoluminescence (PL) as shown in Figure 1d and Figure 1e, respectively. Figure 1d shows the Raman spectrum obtained from monolayer MoS_2 films excited by 514 nm continuous wave laser irradiation at room temperature. The separation between two signature vibrational modes is used to identify the MoS_2 film thickness: the A_1 (out-of-plane) and E'(in-plane) vibrational modes for sub-monolayer (<1L) and monolayer (1L), while the A_{1g} and E_{2g} modes are used for multilayer (ML) MoS_2, respectively. These two $A_1(A_{1g})$ and $E'(E^1_{2g})$ vibrational modes are illustrated in Figure 1f. The A_1 and E' vibrational modes for 1L MoS_2 are located at 404.8 and 386.8 cm^{-1} with peak frequency (cm^{-1}) separations of around 18 cm^{-1}, while those separations for ML MoS_2 are around 19-24 cm^{-1}, depending on the film thickness.[54] Two Raman modes, E^1_{2g} and A_{1g}, exhibit a dependence on layer number, with the frequency of the former decreasing and that of the latter increasing with thickness.[55] From the observed separation of 18 cm^{-1} in Figure 1d, we estimate that our MoS_2 films in the thinnest regions (b) are (sub)monolayer in thickness. In region (c), the films likely exist as quadrilayers (4L) based on the wavenumber difference between the $A_1(A_{1g})$ and $E'(E^1_{2g})$ Raman peaks, as shown in Figure S1. Figure 1e illustrates a room temperature photoluminescence (PL) spectrum of 1L MoS_2 on the SiO_2/Si substrate, where we observe a strong PL signal at 661.8 nm corresponding to the A_1 direct exciton transition at 1.85 eV (670 nm).[10] This PL data is consistent with our Raman spectroscopy observations (Figure 1d) for 1L MoS_2.[57] The strong PL intensity observed is consistent with the high radiative efficiency expected for 1L MoS_2 due to the direct energy gap.[54-56]

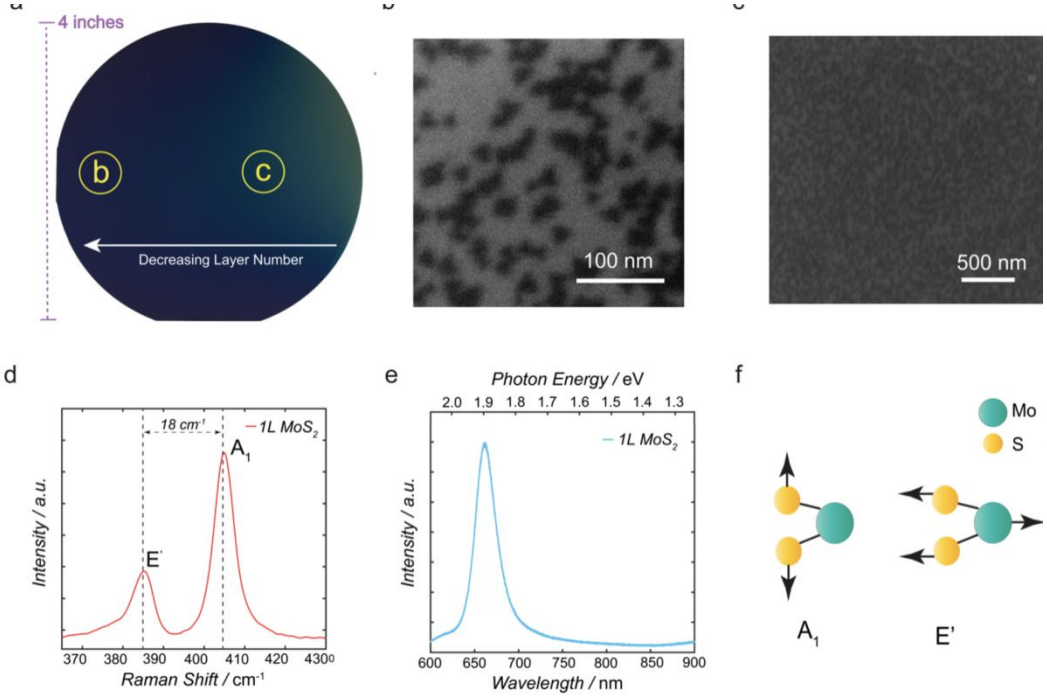

Figure 1. Metal organic chemical vapor deposition (MOCVD)-grown monolayer and multilayer MoS_2 compounds and their characterizations. (a) Monolayer and few-layer MoS_2 flakes were grown on a 4-inch SiO_2/Si substrate. (b) Scanning electron microscopy (SEM) images show the monolayer MoS_2 and (c) multilayer MoS_2 flakes homogeneously deposited on the silicon wafer. (d) Raman and (e) photoluminescence spectra were acquired under 514-nm laser excitation. (f) The in-plane (E') and out-of-plane (A_1) vibration modes that exist in MoS_2 compounds.

To prepare $MoS_{2(1-x)}Se_2x$ compounds, we use an established high-temperature selenization method by flowing selenium vapors reacting with hydrogen in a mixed stream to form H_2Se(g) under a N_2 environment. Figure 2a shows the experimental setup used for the selenization of quadrilayer MoS_2 to form various $MoS_{2(1-x)}Se_{2x}$ alloys (x ranges from 0, 0.12, 0.18, 0.23, 0.26 to 1), where x denotes the atomic fraction of selenium in the alloy. By control of the synthesis temperature, pressure, time, as well as the amount of selenium powder, $MoS_{2(1-x)}Se_2$ with higher selenium fractions ($0.26 < x < 1$) can be further obtained. More synthetic details of the selenization processes are described in the Methods section. Figure 2b shows the trends in the Raman spectra for $MoS_{2(1-x)}Se_{2x}$ films as a function of selenium composition. The Raman data indicates a clear trend associated with the transition with increasing Se composition from pure MoS_2 to alloyed

MoSSe and subsequently to pure $MoSe_2$. The formation of MoSSe alloys is inferred from the presence of Raman peaks located at 287 cm^{-1} and 239 cm^{-1} (denoted as E' and A_1 modes of $MoSe_2$, respectively), which suggest the formation of Mo-Se bonds, along with the weaker signals for MoS_2 at 404.8 cm^{-1} and 386.8 cm^{-1} (assigned to A_1 and E' modes of MoS_2) as the Se composition increases.[58–61] In $MoS_{2(1-x)}Se_{2x}$ alloys for x = 0.12 to 0.26, we observed both MoS_2 and $MoSe_2$ peaks coexisting in the Raman spectra, which clearly shows the evidence of Mo-S and Mo-Se bond formation. Most importantly, no MoS_2 characteristic Raman peaks are shown in $MoSe_2$ (when x=1 in $MoS_{2(1-x)}Se_{2x}$), which indicates selenization process is complete and homogeneous. The signatures associated with MoSSe alloys are accompanied by MoS_2 and $MoSe_2$ Raman signals, which suggests that some portions of the MoS_2 film are selenized to MoSSe. By increasing the selenium composition, full conversion to $MoSe_2$ films is achieved. Notably, we observe an obvious red-shift of the E^1_{2g} mode of MoS_2 with increasing selenium incorporation, indicating the presence of strain in the resultant alloy.[62,63] As the Se content increases in strained regions of the film, we expect that the Mo-S mode would be softened by the interactions between Se and S. On the contrary, in such regions the Se-Mo modes would be strengthened, leading to a red shift in their modal frequencies.[64]

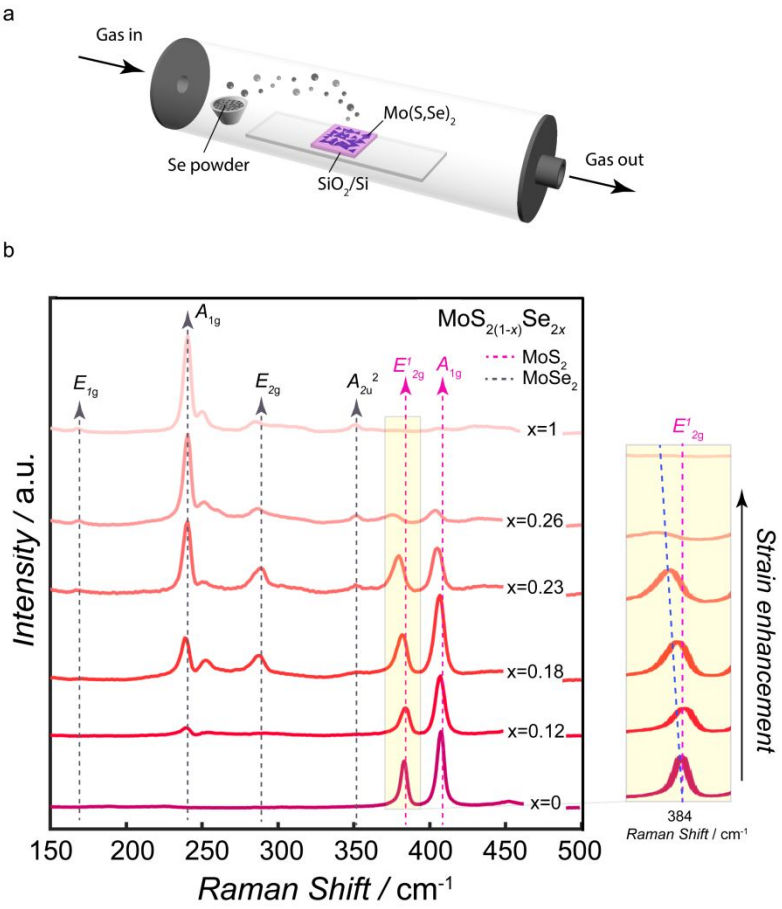

Figure 2. Synthesis of $MoS_{2(1-x)}Se_{2x}$ from pristine MoS_2. (a) Experimental setup of the vapor-phase thermal selenization process. (b) Raman spectroscopy was utilized to examine the formation of $MoS_{2(1-x)}Se_{2x}$ compounds. It shows an evolution of structure and chemical composition from MoS_2 to MoSSe and eventually $MoSe_2$.

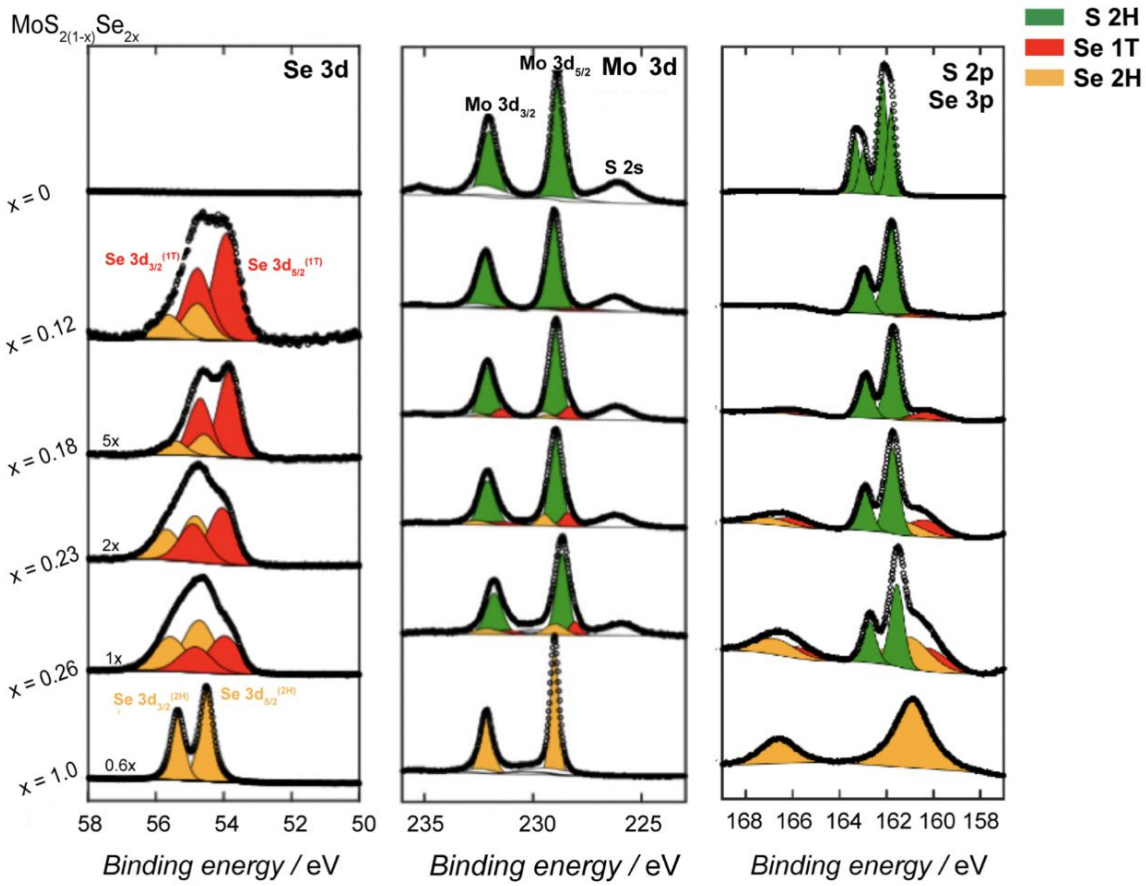

Figure 3. Chemical composition evolution of $MoS_{2(1-x)}Se_{2x}$ as a function of Se concentrations monitored through XPS.

To probe the chemical composition as well as the phases of $MoS_{2(1-x)}Se_2$ heterostructures, we performed X-ray photoelectron spectroscopy (XPS) for $MoS_{2(1-x)}Se_{2x}$ alloys, measuring the Mo 3d, Se 3p, Se 3d and S 2p core levels, as shown in Figure 3. The Se composition in few-layer MoSSe was determined by XPS measurements in which the X-ray penetration depth can generally reach several nanometers to acquire signals from the entire sample. We measured the Se concentrations at various spots in each alloy and averaged the obtained XPS signals over the entire sample. More details of MoSSe alloy compositions are listed in Table S1 in the Supporting Information. No significant change is observed in the Mo 3d core level for MoSSe alloys, yet the Se 3p core level spectra change in both peak shape and energy. As expected, Se 3p peak intensities increase as more selenium is incorporated into the $MoS_{2(1-x)}Se_{2x}$ alloys. This XPS result is consistent with the

Raman measurements in Figure 2. The 2H/1T phase transition has been reported to occur in MoS_2 upon sodium or lithium ion-intercalation, thermal annealing, laser irradiation, or mechanical strain.[65–67] In the present work, we attribute the partial phase transition from 2H to 1T phase in $MoS_{2(1-x)}Se_{2x}$ to the high temperature selenization process.[65–67] To distinguish between the 2H and 1T phases, we examine the X-ray photoemission spectra in the region of coexistence of the 2H and 1T phases, focusing particularly on the Se 3p core level spectra in selenized $MoS_{2(1-x)}Se_{2x}$ alloys at x = 0.12 to 0.26. The Se 3p-2H peaks are located at 55.51 eV and 54.65 eV, while Se 3p-1T peaks are located at 54.69 eV and 53.83 eV binding energy, respectively. Moreover, since the S 2p and Se 3p core levels share a similar binding energy range, the contributions for the Se 3p-1T and Se 3p-2H peaks have been included along with their normalized intensities. The crystal structures of the 2H and 1T phase of MoS_2 exhibit different symmetry, with trigonal prismatic coordinated structure for 2H-MoS_2, and an octahedral coordinated structure for 1T-MoS_2 and the less common distorted 1T'-MoS_2.[68,69] At present, this evidence of a phase transition from MoS_2 to $MoS_{2(1-x)}Se_{2x}$ indicates the breaking of the original symmetry of MoS_2 after selenization, which could potentially change the electronic properties of the alloy materials.[68,69] Notably, although a clear Raman signature of the 1T phase of $MoS_{2(1-x)}Se_{2x}$ is lacking in our samples, our XPS spectra (Figure 3) indicate that the 1T phase is generated upon selenization. The absence of an observed 1T phase in Raman spectra versus observation of the 1T phase in XPS can be attributed to the higher sensitivity of XPS to the 1T phase, which has been shown in earlier studies.[57] The 1T phase of MoX_2 (X = S, Se) is known to be metastable in an air ambient atmosphere, and transformation back into the more stable 2H phase is thermodynamically preferred.[70,71] As to the electronic properties, earlier studies show that the metallic 1T phase of the MoSSe alloy exhibits a higher electrical conductivity as well as enhanced catalytic performance for energy conversion applications.[69,72–74] Corresponding impacts of the 2H → 1T phase transition on the band edge of MoX_2 electronic structures measurements are also expected.[67,75–79] Due to the coexistence of two phases, we expect the interfaces between two the phases to comprise both in-plane and out of plane heterostructures, which further alters and complicates electron transport and the corresponding electronic structures in our alloy samples.

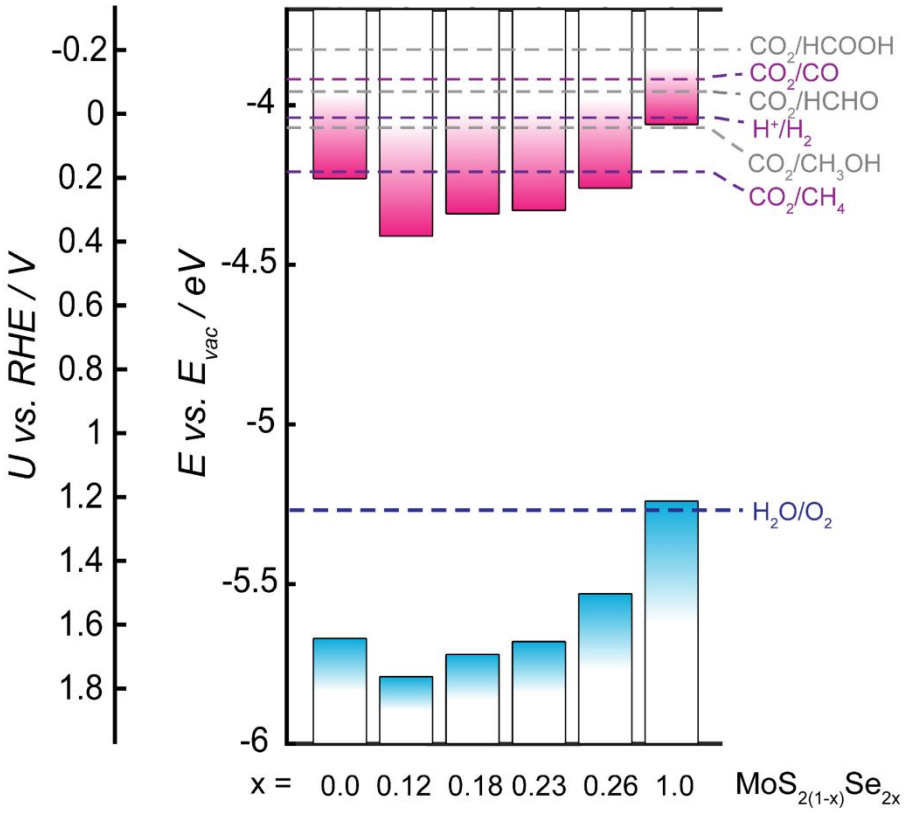

Figure 4. Experimental measurements of electronic band structures of few-layered $MoS_{2(1-x)}Se_{2x}$ films. All the energetic levels are relative to the reduction potentials (vs. RHE) for aqueous CO_2 reduction reaction (pH = 6.8). The valence band edges were derived by XPS and optical band gaps are measured by ellipsometry

To gain insight into the electronic structure, the valence band maxima of $MoS_{2(1-x)}Se_{2x}$ were measured as shown in Figure S2 and Figure S3. Figure 4 illustrates the experimentally-derived energy level diagram depicting the valence band maximum (VBM) and the conduction band minimum (CBM) for our synthesized quadrilayer $MoS_{2(1-x)}Se_{2x}$ alloys (where x ranges from 0 to 1) with respect to the vacuum level, E_{vac} (defined as 0 eV). The $MoS_{2(1-x)}Se_{2x}$ films are synthesized via selenization of the MoS_2 films (see Methods). In this study, our focus was to evaluate the band structure of thicker films for the eventual development of devices, since multiple layers (*e.g.* 4L) are expected to offer more robust stability needed for device applications. Therefore, here we use 4L MoS_2 as the starting material to ensure a continuous film of sufficient thickness on the substrate. The thickness of the MoS_2 film is indicated by the energy difference of the $A_1(A_{1g})$ and $E'(E^1_{2g})$

Raman peaks as shown in Figure S1. In addition, we have depicted the band edge positions relative to the standard reduction potentials, and relative to the reversible hydrogen electrode (RHE), for several CO_2 reduction reactions at a solution of pH = 7 to help visualize the potential utility of $MoS_{2(1-x)}Se_{2x}$ alloys for CO_2R applications. All the band edge positions in Figure 4 were experimentally derived from X-ray photoelectron spectroscopy (XPS) of valence band position and ellipsometry measurements to estimate the bandgap in our synthesized quadrilayer $MoS_{2(1-x)}Se_{2x}$ films (see Methods and Figure S2 and Figure S3). From these data, we observe an increase in the valence band and conduction band edges in $MoS_{2(1-x)}Se_{2x}$ alloys with increasing Se composition. This increase in band edge energy qualitatively parallels the trend predicted by previous calculations for monolayer transition metal dichalcogenides,[80,81] and our measurements show lower valence band and conduction band edges for the alloys relative to MoS_2 and $MoSe_2$. We note that all measured experimental values are relative to the vacuum level.

In our synthesized MoSSe alloys, we observed the coexistence of both 1T and 2H phases. Despite the distinct electronic properties of these two phases,[75,82] the VB and CB positions of the alloy films are expected to be dictated by their overall chemical composition, regardless of the size of individual domains within the MoSSe alloys. We emphasize that the acquired VB and CB data is the result of accumulated signals averaged from several alloyed domains in the XPS and ellipsometry measurements due to the relatively big spot sizes sampled by these two measurements (about 100 μm and 1-5 mm, respectively). The materials characterization was conducted on the entire film and averaged together to elucidate band edge positions. Considering the relatively close correspondence between experiment (Fig. 4) and theory (see Fig. 5), we expect that the 1T impurity does not significantly contribute to the VB and CB edge position.

In general, the electronic structure of $MoS_{2(1-x)}Se_{2x}$ alloys could vary significantly based on the chemical composition, phase distribution, and atomic arrangement in the alloy. Based on our experimental observations, we hypothesized that $MoS_{2(1-x)}Se_{2x}$ alloys could have three possible atomic structures and we performed first-principles density functional theory (DFT) calculations to predict band edge positions (Figure 5) corresponding to each of these structures. The first structure shown in Figure 5a assumes a structure comprising $MoSe_2$ domains within an MoS_2 matrix. The second structure in Figure 5b shows that of a 'vertical heterostructure' with selenium atoms dominating the top layer while the rest of layers underneath has sulfur atoms as the dominant chalcogen species. The third possible structure is a homogeneous alloy, with sulfur and selenium

distributed uniformly throughout the layers. For vertical heterostructures and homogeneous alloys, the conduction band edge becomes progressively more positive as a function of increasing selenium doping. However, in the case of $MoSe_2$ domains embedded in MoS_2, the conduction band edge varies less significantly with increasing Se content and is in all cases more negative than the conduction band edge of the binary alloy structures. This result of the upward trend of the conduction band edges is consistent with prior studies of lateral heterostructures of monolayer MoS_2 and $MoSe_2$.[83,84] These theoretically-predicted trends suggest that our samples may consist of a combination of different types of $MoS_{2(1-x)}Se_{2x}$ structures, which is consistent with our experimental observations of the conduction band edges shown in Figure 4. Based on the calculation results, it is expected to see the upward trend of the VB edges with increasing Se concentration; however, we note that the VB edge positions determined from experiment do not match perfectly with those predicted from DFT calculations. Although the overall trend is in accordance with theoretical predictions, the x = 0.12 sample is clearly an outlier. The discrepancy between experiment and theory for this sample, compared to pure MoS_2, is likely attributable to the coverage of adsorbates (oxygen and/or hydroxyl groups) on the surface of the alloy. The MoS_2 sample is prepared in a single step via MOCVD as opposed to the alloyed samples, which require two steps of thermal cycling at elevated temperature to prepare. Since the alloying selenization procedure is performed via chalcogen ion exchange at an elevated temperature, this process may lead to the introduction of additional defects that serve as sites for adsorption of water or oxygen from the ambient.[85,86] It is known that the adsorbates on MoS_2 can lead to higher work function values as compared to pristine MoS_2.[87] This aspect appears to be the most plausible explanation for why the x = 0.12 alloyed sample has a higher work function than the MoS_2 sample. Despite this small discrepancy between experiment and theory, the overall trend of the shifting VB position with increasing Se content is consistent with theory, confirming that selenization is a viable strategy for tuning the band edges of TMDC materials. We emphasize that this discrepancy between experiment and theory is minor and doesn't affect our general conclusions.

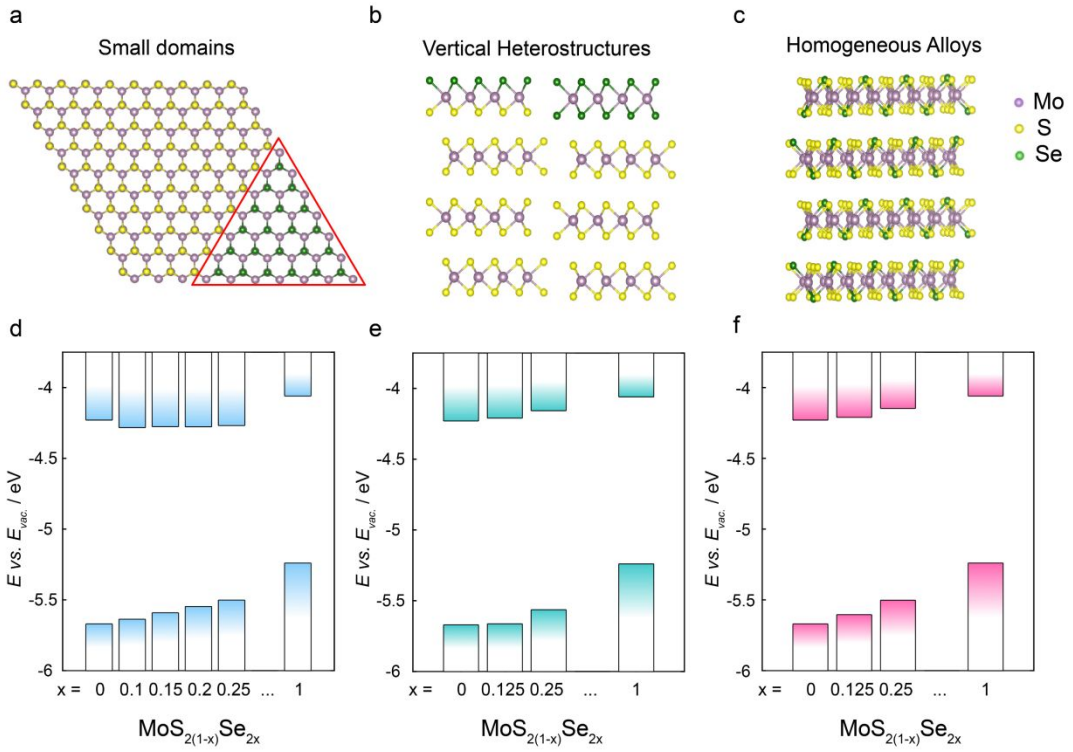

Figure 5. The calculated band edges of three different hypothesized $MoS_{2(1-x)}Se_{2x}$ structures by using first-principles density functional theory (DFT) with van der Waals (vdW) corrections (rev-vdW-DF2) using the Vienna *ab-initio* simulation package (VASP). Three structures include (a) small domains with both MoS_2 and $MoSe_2$, (b) Vertical heterostructures (MoS_2 as the majority and $MoSe_2$ as the topic layer, and (c) homogeneous alloy. (d), (e), (f) are the corresponding calculated band structures of (a), (b) and (c), respectively.

Further insights into the crystalline structure of $MoS_{2(1-x)}Se_{2x}$, were gained from the comparison of Raman spectra with DFT results as shown in Figure 2 and Figure 5, respectively. In Figure 5, the calculated band edge positions of three different proposed structures of $MoS_{2(1-x)}Se_{2x}$ all increase as a function of Se concentration for homogeneous alloys and vertical heterostructures while lateral domains demonstrate a downward shift of the conduction band edges relative to the pristine structures. Additionally, two sets of composition-dependent vibrational modes (Figure 2b) were observed in the Raman spectra from pure MoS_2 (at higher frequency, 350-410 cm^{-1}) and $MoSe_2$ (at lower frequency, 200-300 cm^{-1}), rather than a single set of peaks for ternary MoSSe phases. Such two-mode behavior shown in Raman spectra indicate that our $MoS_{2(1-x)}Se_{2x}$ compounds are likely composed of coexisting MoS_2 and $MoSe_2$ domains (both horizontally

and vertically) instead of a single-phase, atomically-homogeneous, substitutional MoSSe alloy. The above results are consistent with the experimental band edge data in Figure 4. Incorporation of Se into pristine MoS_2 not only changes the macrostructure of $MoS_{2(1-x)}Se_{2x}$, but also generates local strain in the alloy itself, further tailoring the local electronic structure.[88,89] Figure S4 exhibits the calculated the bond angles of pristine MoS_2, $MoSe_2$ and $MoS_{1.5}Se_{0.5}$ alloys (x = 0.25, denoted as 25% small domains to be representative of the ternary alloy) to show the local elemental bonding of Mo to chalcogens (S and Se). Compared with pristine MoS_2 and $MoSe_2$ alloys, the $MoS_{1.5}Se_{0.5}$ alloy consisting of small lateral domains of $MoSe_2$ exhibits observable bond angle changes at the domain interface in the bond angles denoted as A(A'), B, and C, which implies geometric changes in local atomic structure. Furthermore, the heterojunctions in $MoS_{2(1-x)}Se_{2x}$ alloys also introduce strain at the MoS_2/$MoSe_2$ interface. A local phase transition is often accompanied by the existence of local strains, particularly in monolayer or few-layer transition metal dichalcogenide materials.[67] This type of strain has been demonstrated to alter local electronic structure and adsorption energy of the material, ultimately influencing the catalytic activity of TMDC alloys.[90,91] Our correlation of the electronic structure of a series $MoS_{2(1-x)}Se_{2x}$ compounds suggests potential applications for catalysis such as in electrochemical CO_2R. Nevertheless, additional calculations of the adsorption energy, solvation effects, structural phase inhomogeneity, kinetic barriers and activation energy for CO_2R are needed to evaluate the potential catalytic performance of these materials, and will be the subject of ongoing studies.

▪ CONCLUSIONS

In summary, we have synthesized a series of few-layer $MoS_{2(1-x)}Se_{2x}$ alloys through chemical alloying of MOCVD-grown MoS_2 with high-temperature selenization process. Experimental characterization of the $MoS_{2(1-x)}Se_{2x}$ band edges via XPS and ellipsometry indicates that their valence and conduction band edges shift positively with increasing selenium content. The resulting upward shift of their band edges relative to the electrochemical reduction potentials for CO_2 reduction suggests their promise as (photo)electrocatalysts for the CO_2RR. In addition to tuning of band edge energies, local strains within the alloy film may lead to altered catalytic activity. Finally, our experimental observation of band edge tuning through selenium incorporation in MoS_2,

corroborated by calculations, suggest a new approach for tailoring the optoelectronic properties of TMDC alloys.

▪ ASSOCIATED CONTENT

Supporting Information

Raman characterizations of MOCVD-grown MoS_2 on 4-inch SiO_2/Si substrate. Valence band and work function spectra measured by XPS. Extinction coefficient of different $MoS_{2(1-x)}Se_{2x}$ samples. Simulated bond angles of pristine MoS_2, MoSSe and $MoSe_2$ between various bonds, such as S-S, Se-Se, and S-Se in small domain case as well as comparison of calculated bond angles in various compounds. All the chemical compositions of $MoS_{2(1-x)}Se_{2x}$ in this work.

▪ Author information

Corresponding Author

Harry A. Atwater - *Thomas J. Watson Laboratory of Applied Physics, California Institute of Technology, Pasadena, California 91125 United States; Joint Center for Artificial Photosynthesis, California Institute of Technology, Pasadena, California 91125 United States;* orcid.org/0000-0001-9435-0201; Email: haa@caltech.edu

Authors

Yi-Rung Lin - *Thomas J. Watson Laboratory of Applied Physics, California Institute of Technology, Pasadena, California 91125 United States; Joint Center for Artificial Photosynthesis, California Institute of Technology, Pasadena, California 91125 United States; Center for Condensed Matter Sciences, National Taiwan University, No. 1, Sec. 4, Roosevelt Road, Taipei, 10617, Taiwan; Center of Atomic Initiative for New Materials, National Taiwan University, No. 1, Sec. 4, Roosevelt Road, Taipei, 10617, Taiwan;* orcid.org/0000-0003-0331-3822

Wen-Hui Cheng - *Thomas J. Watson Laboratory of Applied Physics, California Institute of Technology, Pasadena, California 91125 United States; Joint Center for Artificial Photosynthesis, California Institute of Technology, Pasadena, California 91125 United States;* orcid.org/0000-0003-3233-4606

Matthias H. Richter – *Joint Center for Artificial Photosynthesis, California Institute of Technology, Pasadena, California 91125 United States; Division of Chemistry and Chemical Engineering, California Institute of Technology, Pasadena, CA 91125, USA;* orcid.org/0000-0003-0091-2045

Joseph S. DuChene - *Thomas J. Watson Laboratory of Applied Physics, California Institute of Technology, Pasadena, California 91125 United States; Joint Center for Artificial Photosynthesis, California Institute of Technology, Pasadena, California 91125 United States;* orcid.org/0000-0002-7145-323X

Elizabeth A. Peterson - *Department of Physics, University of California, Berkeley, California, 94720, USA; Joint Center for Artificial Photosynthesis, Lawrence Berkeley National Laboratory, Berkeley, California 94720, USA;* orcid.org/0000-0001-5379-3604

Cora M. Went - Department of Physics, California Institute of Technology, Pasadena, CA 91125, USA; orcid.org/0000-0001-7737-3348

Zakaria Y. Al Balushi - *Thomas J. Watson Laboratory of Applied Physics, California Institute of Technology, Pasadena, California 91125 United States; The Resnick Sustainability Institute, California Institute of Technology, Pasadena, California 91125 United States;* orcid.org/0000-0003-0589-1618

Deep Jariwala - *Thomas J. Watson Laboratory of Applied Physics, California Institute of Technology, Pasadena, California 91125 United States; # Current address: Electrical and Systems Engineering, University of Pennsylvania, Philadelphia, PA, 19104, USA* orcid.org/0000-0002-3570-8768

Jeffrey B. Neaton - *Department of Physics, University of California, Berkeley, California, 94720, USA; Molecular Foundry, Lawrence Berkeley National Laboratory, Berkeley, California 94720, USA; Kavli Energy NanoSciences Institute at Berkeley, Berkeley, California 94720, USA;* orcid.org/0000-0001-7585-6135

Li-Chyong Chen – *Center for Condensed Matter Sciences, National Taiwan University, No. 1, Sec. 4, Roosevelt Road, Taipei, 10617, Taiwan; Center of Atomic Initiative for New Materials, National Taiwan University, No. 1, Sec. 4, Roosevelt Road, Taipei, 10617, Taiwan;* orcid.org/0000-0001-6373-7729

Harry A. Atwater - *Thomas J. Watson Laboratory of Applied Physics, California Institute of Technology, Pasadena, California 91125 United States; Joint Center for Artificial Photosynthesis, California Institute of Technology, Pasadena, California 91125 United States;* orcid.org/0000-0001-9435-0201; Email: haa@caltech.edu

▪ ACKNOWLEDGEMENTS

This work was performed in the Joint Center for Artificial Photosynthesis, a Department of Energy (DOE) Energy Innovation Hub, supported through the Office of Science of the U.S. Department of energy under Award Number DE-SC0004993. X-ray photoelectron spectroscopy was carried out at the Molecular Materials Research Center of the Beckman Institute of the California Institute of Technology. Y.R.L. acknowledges supports from the Ministry of Science and Technology (MoST), Taiwan. Y.R.L. also acknowledges financial support by the Center of Atomic Initiative for New Materials, National Taiwan University, from the Featured Areas Research Center Program within the framework of the Higher Education Sprout Project by the Ministry of Education in Taiwan (108L9008).

▪ REFERENCES

(1) Mueller, T.; Malic, E. Exciton Physics and Device Application of Two-Dimensional Transition Metal Dichalcogenide Semiconductors. *npj 2D Mater. Appl.* **2018**, *2*, 1–12.

(2) Geng, D.; Yang, H. Y. Recent Advances in Growth of Novel 2D Materials: Beyond Graphene and Transition Metal Dichalcogenides. *Adv. Mater.* **2018**, *30*, 1–23.

(3) Butler, S. Z.; Hollen, S. M.; Cao, L.; Cui, Y.; Gupta, J. A.; Gutiérrez, H. R.; Heinz, T. F.; Hong, S. S.; Huang, J.; Ismach, A. F.; et al. Progress, Challenges, and Opportunities in Two-Dimensional Materials beyond Graphene. *ACS Nano* **2013**, *7*, 2898–2926.

(4) Wang, H.; Li, C.; Fang, P.; Zhang, Z.; Zhang, J. Z. Synthesis, Properties, and Optoelectronic Applications of Two-Dimensional MoS_2 and MoS_2-Based Heterostructures. *Chem. Soc. Rev.* **2018**, *47*, 6101–6127.

(5) Xu, J.; Li, X.; Liu, W.; Sun, Y.; Ju, Z.; Yao, T.; Wang, C.; Ju, H.; Zhu, J.; Wei, S.; et al. Carbon Dioxide Electroreduction into Syngas Boosted by a Partially Delocalized Charge in Molybdenum Sulfide Selenide Alloy Monolayers. *Angew. Chem. Int. Ed.* **2017**, *56*, 9121–9125.

(6) Asadi, M.; Kim, K.; Liu, C.; Addepalli, A. V.; Abbasi, P.; Yasaei, P.; Phillips, P.; Behranginia, A.; Cerrato, J. M.; Haasch, R.; *et* al. Nanostructured Transition Metal Dichalcogenide Electrocatalysts for CO_2 Reduction in Ionic Liquid. *Science* **2016**, *353*, 467–470.

(7) Lewis, N. S.; Ferrer, I. M.; Saadi, F. H.; Francis, S. A.; Brunschwig, B. S.; Torelli, D. A.; McDowell, M. T.; Velazquez, J. M.; John, J.; Zhou, X.; et al. Reduction of Aqueous CO_2 to 1-Propanol at MoS_2 Electrodes. *Chem. Mater.* **2018**, *30*, 4902–4908.

(8) Abbasi, P.; Asadi, M.; Liu, C.; Sharifi-Asl, S.; Sayahpour, B.; Behranginia, A.; Zapol, P.; Shahbazian-Yassar, R.; Curtiss, L. A.; Salehi-Khojin, A. Tailoring the Edge Structure of Molybdenum Disulfide toward Electrocatalytic Reduction of Carbon Dioxide. *ACS Nano* **2017**, *11*, 453–460.

(9) Chan, K.; Tsai, C.; Hansen, H. A.; Nørskov, J. K. Molybdenum Sulfides and Selenides as Possible Electrocatalysts for CO_2 Reduction. *ChemCatChem* **2014**, *6*, 1899–1905.

(10) Asadi, M.; Kumar, B.; Behranginia, A.; Rosen, B. A.; Baskin, A.; Repnin, N.; Pisasale, D.; Phillips, P.; Zhu, W.; Haasch, R.; et al. Robust Carbon Dioxide Reduction on Molybdenum Disulphide Edges. *Nat. Comm.* **2014**, *5*, 1–8.

(11) Ji, Y.; Norskov, J. K.; Chan, K. Scaling Relations on Basal Plane Vacancies of Transition Metal Dichalcogenides for CO_2 Reduction. *J. Phys. Chem. C* **2019**, *123*, 4256–4261.

(12) Tsai, C.; Chan, K.; Nørskov, J. K.; Abild-Pedersen, F. Rational Design of MoS_2 Catalysts: Tuning the Structure and Activity via Transition Metal Doping. *Catal. Sci. Technol.* **2015**, *5*, 246–253.

(13) Yang, L.; Wang, W.; Fu, Q.; Zhang, J.; Xiang, B. $MoS_{2(1-x)}Se_{2x}$ Nanobelts for Enhanced Hydrogen Evolution. *Electrochim. Acta* **2015**, *185*, 236–241.

(14) Gong, Q.; Cheng, L.; Liu, C.; Zhang, M.; Feng, Q.; Ye, H.; Zeng, M.; Xie, L.; Liu, Z.; Li, Y. Ultrathin $MoS_{2(1-x)}Se_{2x}$ Alloy Nanoflakes for Electrocatalytic Hydrogen Evolution Reaction. *ACS Catal.* **2015**, *5*, 2213–2219.

(15) Guan, Z.; Ni, S.; Hu, S. Tunable Electronic and Optical Properties of Monolayer and Multilayer Janus MoSSe as a Photocatalyst for Solar Water Splitting: A First-Principles Study. *J. Phys. Chem. C* **2018**, *122*, 6209–6216.

(16) Haque, F.; Daeneke, T.; Kalantar-zadeh, K.; Ou, J. Z. Two-Dimensional Transition Metal Oxide and Chalcogenide-Based Photocatalysts. *Nano-Micro Lett.* **2018**, *10*, 23.

(17) Zhang, N.; Long, R.; Gao, C.; Xiong, Y. Recent Progress on Advanced Design for Photoelectrochemical Reduction of CO_2 to Fuels. *Sci. China Mater.* **2018**, *61*, 771–805.

(18) Tamirat, A. G.; Rick, J.; Dubale, A. A.; Su, W. N.; Hwang, B. J. Using Hematite for Photoelectrochemical Water Splitting: A Review of Current Progress and Challenges. *Nanoscale Horiz.* **2016**, *1*, 243–267.

(19) Yang, A.; Blancon, J.-C.; Jiang, W.; Zhang, H.; Wong, J.; Yan, E.; Lin, Y.-R.; Crochet, J.; Kanatzidis, M. G.; Jariwala, D.; et al. Giant Enhancement of Photoluminescence Emission in WS_2-Two-Dimensional Perovskite Heterostructures. *Nano Lett.* **2019**, *19*, 4852–4860.

(20) Komsa, H. P.; Krasheninnikov, A. V. Two-Dimensional Transition Metal Dichalcogenide Alloys: Stability and Electronic Properties. *J. Phys. Chem. Lett.* **2012**, *3* , 3652–3656.

(21) Xie, L. M. Two-Dimensional Transition Metal Dichalcogenide Alloys: Preparation, Characterization and Applications. *Nanoscale* **2015**, *7*, 18392–18401.

(22) Zhang, J.; Jia, S.; Kholmanov, I.; Dong, L.; Er, D.; Chen, W.; Guo, H.; Jin, Z.; Shenoy, V. B.; Shi, L.; et al. Janus Monolayer Transition-Metal Dichalcogenides. *ACS Nano* **2017**, *11*, 8192–8198.

(23) Zhou, Z.; Niu, X.; Zhang, Y.; Wang, J. Janus MoSSe/WSeTe Heterostructures: A Direct Z-Scheme Photocatalyst for Hydrogen Evolution. *J. Mater. Chem. A* **2019**, *7*, 21835–21842.

(24) Lei, Y.; Pakhira, S.; Fujisawa, K.; Wang, X.; Iyiola, O. O.; Perea López, N.; Laura Elías, A.; Pulickal Rajukumar, L.; Zhou, C.; Kabius, B.; et al. Low-Temperature Synthesis of Heterostructures of Transition Metal Dichalcogenide Alloys ($W_xMo_{1-X}S_2$) and Graphene with Superior Catalytic Performance for Hydrogen Evolution. *ACS Nano* **2017**, *11*, 5103–

588 5112.
589 (25) Yuan, X.; Yang, M.; Wang, L.; Li, Y. Structural Stability and Intriguing Electronic
590 Properties of Two-Dimensional Transition Metal Dichalcogenide Alloys. *Phys. Chem.*
591 *Chem. Phys.* **2017**, *19*, 13846–13854.
592 (26) Kutana, A.; Penev, E. S.; Yakobson, B. I. Engineering Electronic Properties of Layered
593 Transition-Metal Dichalcogenide Compounds through Alloying. *Nanoscale* **2014**, *6*, 5820–
594 5825.
595 (27) Bogaert, K.; Liu, S.; Liu, T.; Guo, N.; Zhang, C.; Gradečak, S.; Garaj, S. Two-Dimensional
596 $Mo_xW_{1-x}S_2$ Graded Alloys: Growth and Optical Properties. *Sci. Rep.* **2018**, *8*, 2–8.
597 (28) Apte, A.; Krishnamoorthy, A.; Hachtel, J. A.; Susarla, S.; Idrobo, J. C.; Nakano, A.; Kalia,
598 R. K.; Vashishta, P.; Tiwary, C. S.; Ajayan, P. M. Telluride-Based Atomically Thin Layers
599 of Ternary Two-Dimensional Transition Metal Dichalcogenide Alloys. *Chem. Mater.* **2018**,
600 *30*, 7262–7268.
601 (29) Huang, B.; Yoon, M.; Sumpter, B. G.; Wei, S. H.; Liu, F. Alloy Engineering of Defect
602 Properties in Semiconductors: Suppression of Deep Levels in Transition-Metal
603 Dichalcogenides. *Phys. Rev. Lett* **2015**, *115*, 1–5.
604 (30) Wang, Z.; Shen, Y.; Ito, Y.; Zhang, Y.; Du, J.; Fujita, T.; Hirata, A.; Tang, Z.; Chen, M.
605 Synthesizing 1T-1H Two-Phase $Mo_{1-X}W_xS_2$ Monolayers by Chemical Vapor Deposition.
606 *ACS Nano* **2018**, *12*, 1571–1579.
607 (31) Lu, A. Y.; Zhu, H.; Xiao, J.; Chuu, C. P.; Han, Y.; Chiu, M. H.; Cheng, C. C.; Yang, C. W.;
608 Wei, K. H.; Yang, Y.; et al. Janus Monolayers of Transition Metal Dichalcogenides. *Nat.*
609 *Nanotechnol.* **2017**, *12*, 744–749.
610 (32) Lee, J.; Shin, J.-H.; Lee, G.-H.; Lee, C.-H. Two-Dimensional Semiconductor
611 Optoelectronics Based on van Der Waals Heterostructures. *J. Nanomater.* **2016**, *6*, 193.
612 (33) Li, H.; Duan, X.; Wu, X.; Zhuang, X.; Zhou, H.; Zhang, Q.; Zhu, X.; Hu, W.; Ren, P.; Guo,
613 P.; et al. Growth of Alloy $MoS_{2x}Se_{2(1-x)}$ Nanosheets with Fully Tunable Chemical
614 Compositions and Optical Properties. *J. Am. Chem. Soc.* **2014**, *136*, 3756–3759.
615 (34) Zhang, Y.; Chang, T. R.; Zhou, B.; Cui, Y. T.; Yan, H.; Liu, Z.; Schmitt, F.; Lee, J.; Moore,
616 R.; Chen, Y.; et al. Direct Observation of the Transition from Indirect to Direct Bandgap in
617 Atomically Thin Epitaxial $MoSe_2$. *Nat. Nanotechnol.* **2014**, *9*, 111–115.
618 (35) Jin, W.; Yeh, P. C.; Zaki, N.; Zhang, D.; Sadowski, J. T.; Al-Mahboob, A.; Van Der Zande,

A. M.; Chenet, D. A.; Dadap, J. I.; Herman, I. P.; et al. Direct Measurement of the Thickness-Dependent Electronic Band Structure of MoS_2 Using Angle-Resolved Photoemission Spectroscopy. *Phys. Rev. Lett.* **2013**, *111*, 106801.

(36) Kang, J.; Tongay, S.; Zhou, J.; Li, J.; Wu, J. Band Offsets and Heterostructures of Two-Dimensional Semiconductors. *Appl. Phys. Lett.* **2013**, *102*, 012111.

(37) Terrones, H.; López-Urías, F.; Terrones, M. Novel Hetero-Layered Materials with Tunable Direct Band Gaps by Sandwiching Different Metal Disulfides and Diselenides. *Sci. Rep.* **2013**, *3*, 1–7.

(38) Cheiwchanchamnangij, T.; Lambrecht, W. R. L. Quasiparticle Band Structure Calculation of Monolayer, Bilayer, and Bulk MoS_2. *Phys. Rev. B* **2012**, *85*, 1–4.

(39) Böker, T.; Severin, R.; Müller, A.; Janowitz, C.; Manzke, R.; Voß, D.; Krüger, P.; Mazur, A.; Pollmann, J. Band Structure of MoS_2, $MoSe_2$, and A−$MoTe_2$: Angle-Resolved Photoelectron Spectroscopy and Ab Initio Calculations. *Physical Review B* **2001**, *64*, 1–11.

(40) Schouten, K. J. P.; Qin, Z.; Gallent, E. P.; Koper, M. T. M. Two Pathways for the Formation of Ethylene in CO Reduction on Single-Crystal Copper Electrodes. *J. Am. Chem. Soc.* **2012**, *134*, 9864–9867.

(41) Kang, J.; Tongay, S.; Li, J.; Wu, J. Monolayer Semiconducting Transition Metal Dichalcogenide Alloys: Stability and Band Bowing. *J. Appl. Phys.* **2013**, *113*, 143703.

(42) Manzeli, S.; Ovchinnikov, D.; Pasquier, D.; Yazyev, O. V.; Kis, A. 2D Transition Metal Dichalcogenides. *Nat. Rev. Mater.* **2017**, *2*, 17033.

(43) Rasmussen, F. A.; Thygesen, K. S. Computational 2D Materials Database: Electronic Structure of Transition-Metal Dichalcogenides and Oxides. *J. Phys. Chem. C* **2015**, *119*, 13169–13183.

(44) Lee, S.; Zhong, Z. Nanoelectronic Circuits Based on Two-Dimensional Atomic Layer Crystals. *Nanoscale* **2014**, *6*, 13283–13300.

(45) Haque, F.; Daeneke, T.; Kalantar-zadeh, K.; Ou, J. Z. Two-Dimensional Transition Metal Oxide and Chalcogenide-Based Photocatalysts. *Nano-Micro Lett.* **2018**, *10*, 23.

(46) Zhang, C.; Gong, C.; Nie, Y.; Min, K. A.; Liang, C.; Oh, Y. J.; Zhang, H.; Wang, W.; Hong, S.; Colombo, L.; et al. Systematic Study of Electronic Structure and Band Alignment of Monolayer Transition Metal Dichalcogenides in Van Der Waals Heterostructures. *2D Mater.* **2017**, *4*, 015026.

(47) Thygesen, K. S. Calculating Excitons, Plasmons, and Quasiparticles in 2D Materials and van Der Waals Heterostructures. *2D Mater.* **2017**, *4*, 022004.

(48) Dirac, P. A. M. On the Theory of Quantum Mechanics. *P. Roy. Soc. A-Mat. Phy.* **1926**, *112*, 661–677.

(49) Kresse, G.; Joubert, D. From Ultrasoft Pseudopotentials to the Projector Augmented-Wave Method. *Phys. Rev. B* **1999**, *59*, 1758.

(50) Kresse, G.; Furthmiiller, J. Efficiency of Ab-Initio Total Energy Calculations for Metals and Semiconductors Using a Plane-Wave Basis Set. *Comput. Mater. Sci.* **1996**, *6*, 15–50.

(51) Kresse, G.; Furthmüller, J. Efficient Iterative Schemes for Ab Initio Total-Energy Calculations Using a Plane-Wave Basis Set. *Phys. Rev. B* **1996**, *54*, 11169–11186.

(52) Perdew, J. P.; Burke, K.; Ernzerhof, M. Generalized Gradient Approximation Made Simple. *Phys. Rev. Lett.* **1996**, *77*, 3865–3868.

(53) Hamada, I. Van Der Waals Density Functional Made Accurate. *Phys. Rev. B* **2014**, *89*, 121103.

(54) Li, H.; Zhang, Q.; Yap, C. C. R.; Tay, B. K.; Edwin, T. H. T.; Olivier, A.; Baillargeat, D. From Bulk to Monolayer MoS_2: Evolution of Raman Scattering. *Adv. Funct. Mater.* **2012**, *22*, 1385–1390.

(55) Lee, C.; Yan, H.; Brus, L. E.; Heinz, T. F.; Hone, Ḱ. J.; Ryu, S. Anomalous Lattice Vibrations of Single- and Few-Layer MoS_2. *ACS Nano* **2010**, *4*, 2695–2700.

(56) Livneh, T.; Sterer, E. Resonant Raman Scattering at Exciton States Tuned by Pressure and Temperature in 2H -MoS_2. *Phys. Rev. B* **2010**, *81*, 1–9.

(57) Splendiani, A.; Sun, L.; Zhang, Y.; Li, T.; Kim, J.; Chim, C. Y.; Galli, G.; Wang, F. Emerging Photoluminescence in Monolayer MoS_2. *Nano Lett.* **2010**, *10*, 1271–1275.

(58) Tonndorf, P.; Schmidt, R.; Böttger, P.; Zhang, X.; Börner, J.; Liebig, A.; Albrecht, M.; Kloc, C.; Gordan, O.; Zahn, D. R. T.; et al. Photoluminescence Emission and Raman Response of Monolayer MoS_2, $MoSe_2$, and WSe_2. *Opt. Express* **2013**, *21*, 4908–4916.

(59) Late, D. J.; Shirodkar, S. N.; Waghmare, U. V.; Dravid, V. P.; Rao, C. N. R. Thermal Expansion, Anharmonicity and Temperature-Dependent Raman Spectra of Single- and Few-Layer $MoSe_2$ and WSe_2. *ChemPhysChem* **2014**, *15*, 1592–1598.

(60) Lee, C.; Yan, H.; Brus, L. E.; Heinz, T. F.; Hone, J.; Ryu, S. Anomalous Lattice Vibrations of Single- and Few-Layer MoS_2. *ACS Nano* **2010**, *4*, 2695–2700.

(61) Wirtz, L.; Molina-Sanchez, A. Phonons in Single and Few-Layer MoS_2 and WS_2. *Phys. Rev. B* **2011**, *84*, 155413.

(62) Castellanos-Gomez, A.; Roldán, R.; Cappelluti, E.; Buscema, M.; Guinea, F.; Van Der Zant, H. S. J.; Steele, G. A. Local Strain Engineering in Atomically Thin MoS_2. *Nano Lett.* **2013**, *13*, 5361–5366.

(63) Dhakal, K. P.; Roy, S.; Jang, H.; Chen, X.; Yun, W. S.; Kim, H.; Lee, J.; Kim, J.; Ahn, J. H. Local Strain Induced Band Gap Modulation and Photoluminescence Enhancement of Multilayer Transition Metal Dichalcogenides. *Chem. Mater.* **2017**, *29*, 5124–5133.

(64) Li, H.; Duan, X.; Wu, X.; Zhuang, X.; Zhou, H.; Zhang, Q.; Zhu, X.; Pan, A.; Duan, X. Growth of Alloy $MoS_{2x}Se_{2(1-x)}$ Nanosheets with Fully Tunable Chemical Compositions and Optical Properties. *J. Am. Chem. Soc.* **2014**, *136*, 3756–3759.

(65) Duerloo, K. A. N.; Li, Y.; Reed, E. J. Structural Phase Transitions in Two-Dimensional Mo- and W-Dichalcogenide Monolayers. *Nat. Comm.* **2014**, *5*, 4214.

(66) Huang, X.; Yang, Z.; Zhang, H.; Zhao, M.; Xiong, Q.; Du, Y.; Chen, J.; Zhang, Q.; Yu, Y.; He, Q.; et al. High Phase-Purity 1T′-MoS_2- and 1T′-$MoSe_2$-Layered Crystals. *Nat. Chem.* **2018**, *10*, 638–643.

(67) Lin, Y. C.; Dumcenco, D. O.; Huang, Y. S.; Suenaga, K. Atomic Mechanism of the Semiconducting-to-Metallic Phase Transition in Single-Layered MoS_2. *Nat. Nanotechnol.* **2014**, *9*, 391–396.

(68) Kappera, R.; Voiry, D.; Yalcin, S. E.; Branch, B.; Gupta, G.; Mohite, A. D.; Chhowalla, M. Phase-Engineered Low-Resistance Contacts for Ultrathin MoS_2 Transistors. *Nat. Mater.* **2014**, *13*, 1128–1134.

(69) Voiry, D.; Mohite, A. D.; Chhowalla, M. Phase Engineering of Transition Metal Dichalcogenides. *Chem. Soc. Rev.* **2015**, *44*, 2702–2712.

(70) Acerce, M.; Voiry, D.; Chhowalla, M. Metallic 1T Phase MoS_2 Nanosheets as Supercapacitor Electrode Materials. *Nat. Nanotechnol.* **2015**, *10*, 313–318.

(71) Yu, Y., Nam, G., He, Q. et al. High Phase-Purity 1T′-MoS_2- and 1T′-$MoSe_2$-Layered Crystals. *Nat. Chem.* **2018**, *10*, 638–643.

(72) Li, H.; Zhang, Q.; Duan, X.; Wu, X.; Fan, X.; Zhu, X.; Zhuang, X.; Hu, W.; Zhou, H.; Pan, A.; et al. Lateral Growth of Composition Graded Atomic Layer $MoS_{2(1-x)}Se_{2x}$ Nanosheets. *J. Am. Chem. Soc.* **2015**, *137*, 5284–5287.

(73) Lukowski, M. A.; Daniel, A. S.; Meng, F.; Forticaux, A.; Li, L.; Jin, S. Enhanced Hydrogen Evolution Catalysis from Chemically Exfoliated Metallic MoS_2 Nanosheets. *J. Am. Chem. Soc.* **2013**, *135*, 10274–10277.

(74) Shi, S.; Sun, Z.; Hu, Y. H. Synthesis, Stabilization and Applications of 2-Dimensional 1T Metallic MoS_2. *J. Mater. Chem. A* **2018**, *6*, 23932–23977.

(75) Jiao, Y.; Hafez, A. M.; Cao, D.; Mukhopadhyay, A.; Ma, Y.; Zhu, H. Metallic MoS_2 for High Performance Energy Storage and Energy Conversion. *Small* **2018**, *14*, 1–20.

(76) Zhao, W.; Pan, J.; Fang, Y.; Che, X.; Wang, D.; Bu, K.; Huang, F. Metastable MoS_2: Crystal Structure, Electronic Band Structure, Synthetic Approach and Intriguing Physical Properties. *Chem. Eur. J.* **2018**, *24*, 15942–15954.

(77) Mann, J.; Ma, Q.; Odenthal, P. M.; Isarraraz, M.; Le, D.; Preciado, E.; Barroso, D.; Yamaguchi, K.; Von Son Palacio, G.; Nguyen, A.; et al. 2-Dimensional Transition Metal Dichalcogenides with Tunable Direct Band Gaps: $MoS_{2(1-x)}Se_{2x}$ Monolayers. *Adv. Mater.* **2014**, *26*, 1399–1404.

(78) Ouyang, B.; Chen, S.; Jing, Y.; Wei, T.; Xiong, S.; Donadio, D. Enhanced Thermoelectric Performance of Two Dimensional MS_2 (M = Mo, W) through Phase Engineering. *J. Materiomics* **2018**, *4*, 329–337.

(79) Ma, F.; Gao, G.; Jiao, Y.; Gu, Y.; Bilic, A.; Zhang, H.; Chen, Z.; Du, A. Predicting a New Phase (T″) of Two-Dimensional Transition Metal Di-Chalcogenides and Strain-Controlled Topological Phase Transition. *Nanoscale* **2016**, *8*, 4969–4975.

(80) Kang, J.; Tongay, S.; Li, J.; Wu, J. Monolayer Semiconducting Transition Metal Dichalcogenide Alloys: Stability and Band Bowing. *J. Appl. Phys.* **2013**, *113*, 143703.

(81) Mann, J.; Ma, Q.; Odenthal, P. M.; Isarraraz, M.; Le, D.; Preciado, E.; Barroso, D.; Yamaguchi, K.; Von Son Palacio, G.; Nguyen, A.; et al. 2-Dimensional Transition Metal Dichalcogenides with Tunable Direct Band Gaps: $MoS_{2(1-x)}$ Se_{2x} Monolayers - Supp Info. *Adv. Mater.* **2014**, *26*, 1399–1404.

(82) Empante, T. A.; Zhou, Y.; Klee, V.; Nguyen, A. E.; Lu, I. H.; Valentin, M. D.; Naghibi Alvillar, S. A.; Preciado, E.; Berges, A. J.; Merida, C. S.; et al. Chemical Vapor Deposition Growth of Few-Layer $MoTe_2$ in the 2H, 1T′, and 1T Phases: Tunable Properties of $MoTe_2$ Films. *ACS Nano* **2017**, *11*, 900–905.

(83) Mahjouri-Samani, M.; Lin, M. W.; Wang, K.; Lupini, A. R.; Lee, J.; Basile, L.; Boulesbaa,

A.; Rouleau, C. M.; Puretzky, A. A.; Ivanov, I. N.; et al. Patterned Arrays of Lateral Heterojunctions within Monolayer Two-Dimensional Semiconductors. *Nat. Comm.* **2015**, *6*, 7749.

(84) Bellus, M. Z.; Mahjouri-Samani, M.; Lane, S. D.; Oyedele, A. D.; Li, X.; Puretzky, A. A.; Geohegan, D.; Xiao, K.; Zhao, H. Photocarrier Transfer across Monolayer MoS_2-$MoSe_2$ Lateral Heterojunctions. *ACS Nano* **2018**, *12*, 7086–7092.

(85) Nan, H.; Wang, Z.; Wang, W.; Liang, Z.; Lu, Y.; Chen, Q.; He, D.; Tan, P.; Miao, F.; Wang, X.; et al. Strong Photoluminescence Enhancement of MoS_2 through Defect Engineering and Oxygen Bonding. *ACS Nano* **2014**, *8*, 5738–5745.

(86) Liu, H.; Han, N.; Zhao, J. Atomistic Insight into the Oxidation of Monolayer Transition Metal Dichalcogenides: From Structures to Electronic Properties. *RSC Advances* **2015**, *5*, 17572–17581.

(87) Kim, J. H.; Lee, J.; Kim, J. H.; Hwang, C. C.; Lee, C.; Park, J. Y. Work Function Variation of MoS_2 Atomic Layers Grown with Chemical Vapor Deposition: The Effects of Thickness and the Adsorption of Water/Oxygen Molecules. *Appl. Phys. Lett.* **2015**, *106*, 251606.

(88) Conley, H. J.; Wang, B.; Ziegler, J. I.; Haglund, R. F.; Pantelides, S. T.; Bolotin, K. I. Bandgap Engineering of Strained Monolayer and Bilayer MoS_2. *Nano Lett.* **2013**, *13*, 3626–3630.

(89) He, K.; Poole, C.; Mak, K. F.; Shan, J. Experimental Demonstration of Continuous Electronic Structure Tuning via Strain in Atomically Thin MoS_2. *Nano Lett.* **2013**, *13*, 2931–2936.

(90) Shown, I.; Samireddi, S.; Chang, Y. C.; Putikam, R.; Chang, P. H.; Sabbah, A.; Fu, F. Y.; Chen, W. F.; Wu, C. I.; Yu, T. Y.; et al. Carbon-Doped SnS_2 Nanostructure as a High-Efficiency Solar Fuel Catalyst under Visible Light. *Nat. Comm.* **2018**, *9*, 169.

(91) Tan, Y.; Liu, P.; Chen, L.; Cong, W.; Ito, Y.; Han, J.; Guo, X.; Tang, Z.; Fujita, T.; Hirata, A.; et al. Monolayer MoS_2 Films Supported by 3D Nanoporous Metals for High-Efficiency Electrocatalytic Hydrogen Production. *Adv. Mater.* **2014**, *26*, 8023–8028.

Table of Contents Figure